Three-dimensional cohesive fracture modeling of non-planar crack growth using adaptive FE technique

A.R. Khoei [a,*], H. Moslemi [b], M. Sharifi [a]

[a] Center of Excellence in Structures and Earthquake Engineering, Department of Civil Engineering, Sharif University of Technology, P.O. Box. 11365-9313, Tehran, Iran
[b] Department of Civil Engineering, Engineering Faculty, Shahed University, P.O. Box 18155/159, Tehran, Iran

ABSTRACT

In this paper, the three-dimensional adaptive finite element modeling is presented for cohesive fracture analysis of non-planer crack growth. The technique is performed based on the Zienkiewicz–Zhu error estimator by employing the modified superconvergent patch recovery procedure for the stress recovery. The Espinosa–Zavattieri bilinear constitutive equation is used to describe the cohesive tractions and displacement jumps. The 3D cohesive fracture element is employed to simulate the crack growth in a non-planar curved pattern. The crack growth criterion is proposed in terms of the principal stress and its direction. Finally, several numerical examples are analyzed to demonstrate the validity and capability of proposed computational algorithm. The predicted crack growth simulation and corresponding load-displacement curves are compared with the experimental and other numerical results reported in literature.

© 2012 Elsevier Ltd. All rights reserved.

1. Introduction

The simulation of crack propagation in continuum mechanics by linear elastic fracture mechanics (LEFM) is well established when the size of nonlinear zone at the crack tip is small compared to the size of crack and the size of specimen (Bažant and Planas, 1998). If the size of fracture process zone is not negligible, the cohesive zone modeling (CZM) approach has been developed as one of the most effective techniques for nonlinear fracture processes and is now widely implemented in finite elements. The cohesive fracture model is able to adequately predict the behavior of uncracked structures, including those with blunt notches. The cohesive fracture element can be used to describe the cohesive forces that occur when the bulk finite elements near the crack tip zone are being pulled apart (Fig. 1). The implementation of cohesive fracture model in crack propagation problems was applied from the early classical models of Dugdale (1960) for the analysis of brittle materials and Barrenblatt (1962) for the analysis of ductile materials. Willis (1967) compared these classic models with the linear elastic model of Griffith (1920) and presented that they are agreed when the cohesive forces act only on a short range. Hillerborg et al. (1976) developed an appropriate numerical incor-poration of cohesive zones into the finite element method introducing the concept of fracture energy for quasi-brittle materials.

The cohesive zone models are typically expressed as the functions of normal and tangential traction–separation relationship. There are various forms of traction–separation functions, such as the polynomial and exponential equations. The polynomial and exponential functions were first proposed by Needleman (1990) using a characteristic length into the formulation. The polynomial shaped traction separation law was modified by Tvergaard (1990) to consider both the normal and tangential separation modes. Tvergaard and Hutchinson (1992, 1996) proposed a trapezoidal type of CZM to study the crack growth resistance in elastic-plastic solids. Camacho and Ortiz (1996) used an adaptation of linear type of CZM with an additional fracture criterion to simulate the multiple crack growth along arbitrary paths under impact damage in brittle materials. Nguyen et al. (2001) proposed a cohesive fracture model based on the unloading-reloading hysteresis for fatigue crack growth. Elices et al. (2001) proposed an inverse analysis procedure to determine the softening function of cohesive model and applied the model to different materials; such as concrete, glassy polymer and steel. Chandra et al. (2002) demonstrated that the form of traction–separation equations for cohesive zone models plays a critical role in determining the macroscopic mechanical response of the system and is sometimes even more important than the value of the tensile strength. Wnuk and Legat (2002) proposed a cohesive zone model to describe the distribution of cohesive
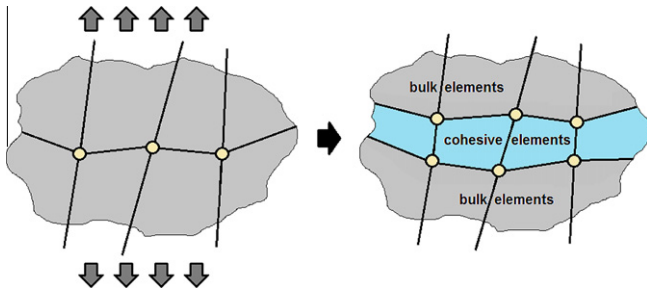
Fig. 1. Implementation of cohesive elements into the bulk FE elements.

forces within the internally structured nonlinear zone using the triaxiality parameter. Espinosa and Zavattieri (2003) proposed a bilinear model to study the material micro-structures subjected to quasi-static and dynamic loading. Song et al. (2006) presented that the bilinear model reduces the artificial compliance in the intrinsic cohesive zone model efficiently.

A key point in the modeling of crack growth is the accuracy of numerical computation due to mesh discretization. In order to overcome the limitations of initial discretisation and to represent the arbitrary crack growth, the mesh adaptive procedure is an appropriate technique. The accuracy of computed crack trajectory is directly linked to the accuracy of numerical computation of local parameters. Adaptive mesh technique can be efficiently used to minimize the error with reasonable computational costs. Carranza et al. (1997) applied the adaptive remeshing technique in the cohesive zone model to present the quasi-static creep crack growth within a moving-grid finite element model. Prasad and Krishna-moorthy (2001) presented a mesh-adaptive strategy based on the Zienkiewicz–Zhu error estimator to analyze the first fracture mode in cement-based materials. Schrefler et al. (2006) developed an adaptive finite element formulation for cohesive fracture zone, which incorporates the solid and fluid phases together with a tem-perature field. They simulated the solid behavior with a fully cou-pled cohesive-fracture discrete model and applied a systematic local remeshing of the domain and a corresponding change of fluid and thermal boundary conditions. An adaptive finite element pro-cedure was presented by Khoei et al. (2008, 2009) in modeling of 2D mixed-mode crack propagations via the modified superconver-gent path recovery technique. Geißler et al. (2010) presented a new algorithmic which allows an adaptive incorporation of the cohesive elements depending on a crack growth criterion for structures with low crack growth rates.

Up to date, the most computational simulation of cohesive crack propagation has been presented in two-dimensional cases, and less numerical modeling has been reported in three-dimen-sional crack propagation of cohesive zone models. Ortiz and Pan-dolfi (1999) developed a three-dimensional finite-deformation cohesive element based on the irreversible cohesive laws for track-ing of dynamically growing cracks. Foulk et al. (2000) presented a formulation for the three-dimensional cohesive zone model ap-plied to a nonlinear finite element algorithm. Ruiz et al. (2001) pro-posed the linear extrinsic cohesive formulation to simulate the process of combined tension-shear damage and mixed-mode frac-ture in dynamic loading. A viscosity-regularized continuum dam-age constitutive model was applied by Areias and Belytschko (2005) within the extended finite element formulation in the reg-ularized crack-band model. Gasser and Holzapfel (2006) combined the cohesive crack concept with the partition of unity finite ele-ment method to predict the closed 3D crack surface based on a two-step algorithm for tracking the crack path, where the predictor step was used to define the discontinuity according to the non-lo-cal failure criterion and the corrector step was employed to draw

the non-local information of existing discontinuity. The mixed interface finite element method was introduced by Lorentz (2008) for three-dimensional cohesive model to discretize the crack paths, the degrees of freedom of which consist in the dis-placement on both crack lips and the density of cohesive forces. The model was used to enable an exact treatment of multi-valued cohesive laws, such as the initial adhesion, contact conditions, pos-sible rigid unloading, etc, without the penalty regularization.

In the present paper, a fully three-dimensional cohesive zone model is developed and applied to simulate the non-planar crack propagation problems. In order to reduce the discretization error to an acceptable value, an adaptive finite element method is em-ployed on the basis of weighted-SPR technique. The outline of the paper is as follows; a three-dimensional interface model is pre-sented in Section 2 in modeling of the cohesive zone behavior. This section includes the bilinear traction–separation law in the cohe-sive zone and its implantation in the FEM technique. Section 3 demonstrates the 3D crack propagation criterion to allocate the cohesive zone elements in the appropriate directions. Section 4 presents the error control process using an effective statistical technique. In Section 5, several practical and complex 3D crack growth simulations are analyzed to illustrate the validity and accu-racy of the proposed computational algorithm. Finally, Section 6 is devoted to conclusion remarks.

2. Cohesive fracture model

In order to model the cohesive zone near the crack tip in finite element formulation, the three-dimensional node-to-node cohe-sive element is employed. The cohesive element is implemented between the real crack tip and the fictitious crack tip where the cohesive zone is separated from the uncracked zone. The cohesive elements are inserted between the top and bottom nodal points to monitor the surfaces of the fictitious crack. When the cohesive ele-ments are constructed, appropriate integration points within the cohesive element become active and the cohesive behavior is taken into account. The cohesive behavior is mainly affected by the cohe-sive parameters such as the cohesive strength and cohesive energy fracture. A bilinear cohesive law is implemented in the cohesive zone, which is described in the next section. The cohesive model is applied into the FE context to obtain a general 3D formulation for the stiffness matrix of cohesive zone elements. It is assumed that no contact is occurred between the crack faces and the contact between the crack faces was controlled during the crack propagation.

2.1. Bilinear cohesive zone model

In this section, a bilinear traction–separation law is used to model the cohesive zone behavior near the crack tip. This model is originally proposed by Espinosa and Zavattieri (2003) and then applied by Song et al. (2006) in 2D cohesive model. This model can efficiently reduce the artificial compliance observed in the cohesive zone. The initial slope of the cohesive law prevents the conflict between the cohesive elements and the continuum body. The descending part of the cohesive law simulates the softening behavior due to the growth of voids. These two distinctive parts are separated by a dimensionless displacement called as the criti-cal separation λ_{cr}. The cohesive law is defined in the term of dimen-sionless effective separation, given by

$$\lambda_e = \sqrt{(\delta_n/\delta_C)^2 + (\delta_s/\delta_C)^2 + (\delta_p/\delta_C)^2} \tag{1}$$

where δ_n is the normal separation and δ_s and δ_p are the tangential separations in local coordinate system directions s and p. The local axes n, s and p are the right-handed coordinate system at the

cohesive zone. In above relation, δ_C denotes the ultimate separation which is related to the stress free state and complete separation of cohesive zone. This parameter is usually determined from the cohesive fracture energy G_C. These two parameters G_C and δ_C can be related by the equilibrium between the area under the cohesive stress-separation diagram and the cohesive fracture energy, i.e.

$$G_C = \frac{1}{2}\sigma_C \delta_C \tag{2}$$

where σ_C is a characteristic property of material in the cohesive zone, which represents the cohesive strength. The cohesive strength and cohesive fracture energy are two influential parameters which control the response of the model in the cohesive zone and are usually determined from experimental results. Depending on the value of effective separation λ_e, it may follow either the initial linear, or the final softening part of the cohesive law. In the case of $\lambda_e \leqslant \lambda_{cr}$, the normal cohesive stress t_n and the tangential cohesive stresses t_s and t_p are linear functions of the corresponding normalized separations defined as

$$t_n = \frac{\sigma_C}{\lambda_{cr}}\left(\frac{\delta_n}{\delta_C}\right), \quad t_s = \frac{\sigma_C}{\lambda_{cr}}\left(\frac{\delta_s}{\delta_C}\right), \quad t_p = \frac{\sigma_C}{\lambda_{cr}}\left(\frac{\delta_p}{\delta_C}\right) \tag{3}$$

If the effective separation exceeds the critical separation, i.e. $\lambda_e > \lambda_{cr}$, the cohesive zone follows the softening part and the cohesive stress gradually vanishes while approaching to the unity. The proportion between the normal and shear cohesive stresses depends on the proportion between the normal and tangential separations. Hence, the cohesive law in this case can be given as

$$t_n = \frac{\sigma_C}{\lambda_e}\frac{1-\lambda_e}{1-\lambda_{cr}}\left(\frac{\delta_n}{\delta_C}\right), \quad t_s = \frac{\sigma_C}{\lambda_e}\frac{1-\lambda_e}{1-\lambda_{cr}}\left(\frac{\delta_s}{\delta_C}\right),$$
$$t_p = \frac{\sigma_C}{\lambda_e}\frac{1-\lambda_e}{1-\lambda_{cr}}\left(\frac{\delta_p}{\delta_C}\right) \tag{4}$$

The above expression cannot be applied in the unloading phase. If the cohesive zone is in the softening zone ($\lambda_e > \lambda_{cr}$) and the model is unloaded ($\dot{\lambda}_e \leqslant 0$), the above equation states that the cohesive stress increases by decreasing the separation that is not acceptable physically. In this case, Eq. (4) can be rewritten as

$$t_n = \frac{\sigma_C}{\lambda_{\max}}\frac{1-\lambda_{\max}}{1-\lambda_{cr}}\left(\frac{\delta_n}{\delta_C}\right), \quad t_s = \frac{\sigma_C}{\lambda_{\max}}\frac{1-\lambda_{\max}}{1-\lambda_{cr}}\left(\frac{\delta_s}{\delta_C}\right),$$
$$t_p = \frac{\sigma_C}{\lambda_{\max}}\frac{1-\lambda_{\max}}{1-\lambda_{cr}}\left(\frac{\delta_p}{\delta_C}\right) \tag{5}$$

where $\lambda_{\max}$ is the maximum effective separation, in which the cohesive elements experience before unloading. Since the effective separation λ_e is affected by the normal and tangential separations, the total effective separation can be decomposed into the normal effective separation λ_n and the tangential effective separation λ_s defined as

$$\lambda_n = \delta_n/\delta_C, \quad \lambda_s = \sqrt{(\delta_s/\delta_C)^2 + (\delta_p/\delta_C)^2} \tag{6}$$

It is obvious from Eqs. (1) and (6) that the normal and tangential effective separations can be related as

$$\lambda_e^2 = \lambda_n^2 + \lambda_s^2 \tag{7}$$

Depending on the proportions between the normal and tangential separations, the cohesive stress-separation relation may take different forms. For example the normal stress-separation relation has the bilinear behavior when no shear separation is occurred in the cohesive element. However, the occurrence of shear separation causes the nonlinearity in the cohesive stress-separation relationship. Fig. 2 illustrates the normal cohesive stress-separation relation at different shear separations. It can be observed from this figure that the linear part is excluded when the effective shear
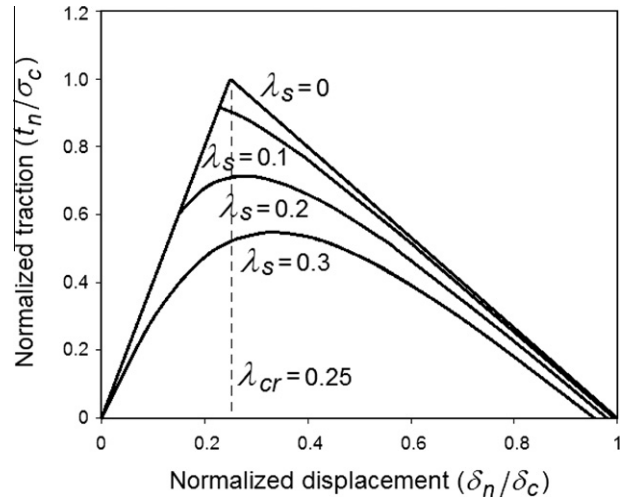

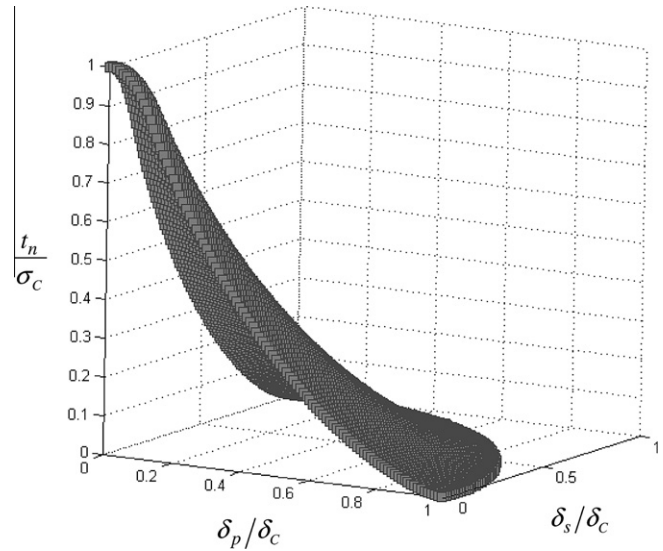**Fig. 2.** The normal separation–traction cohesive law for different shear separations.

Fig. 3. The maximum cohesive normal traction diagram.

separation λ_s exceeds the critical separation λ_{cr}. Obviously, the maximum normal cohesive stress reduces by increasing the proportion of shear separation, since the proportion of normal separation decreases, and in contrast the shear cohesive stress increases. Thus, there is a nonlinear interaction between the normal cohesive stress and the shear separation. Fig. 3 presents this nonlinear relationship between the maximum normal cohesive stress and shear separations in s and p directions.

Since the cohesive stress is related to the separation in cohesive model, the cohesive stress must be differentiated with respect to the separation in order to obtain the tangential modulus matrix of material in cohesive zone. If $\lambda_e \leqslant \lambda_{cr}$, the cohesive material matrix C_f can be obtained from Eq. (3) as

$$C_f = \begin{bmatrix} C_{nn} & C_{ns} & C_{np} \\ C_{sn} & C_{ss} & C_{sp} \\ C_{pn} & C_{ps} & C_{pp} \end{bmatrix} = \begin{bmatrix} \frac{\partial t_n}{\partial \delta_n} & \frac{\partial t_n}{\partial \delta_s} & \frac{\partial t_n}{\partial \delta_p} \\ \frac{\partial t_s}{\partial \delta_n} & \frac{\partial t_s}{\partial \delta_s} & \frac{\partial t_s}{\partial \delta_p} \\ \frac{\partial t_p}{\partial \delta_n} & \frac{\partial t_p}{\partial \delta_s} & \frac{\partial t_p}{\partial \delta_p} \end{bmatrix} = \begin{bmatrix} \frac{\sigma_C}{\lambda_{cr}\delta_C} & 0 & 0 \\ 0 & \frac{\sigma_C}{\lambda_{cr}\delta_C} & 0 \\ 0 & 0 & \frac{\sigma_C}{\lambda_{cr}\delta_C} \end{bmatrix}$$
$$\tag{8}$$

If $\lambda_e > \lambda_{cr}$, the components of cohesive material matrix can be obtained from Eq. (4) as

$$C_f = \begin{bmatrix} C_{nn} & C_{ns} & C_{np} \\ C_{sn} & C_{ss} & C_{sp} \\ C_{pn} & C_{ps} & C_{pp} \end{bmatrix} = \begin{bmatrix} -\frac{\sigma_C}{\delta_C(1-\lambda_{cr})}\left(1 - \frac{1}{\lambda_e} + \frac{1}{\lambda_e^3}\left(\frac{\delta_n}{\delta_C}\right)^2\right) & -\frac{\sigma_C}{\delta_C(1-\lambda_{cr})}\left(\frac{1}{\lambda_e^3}\right)\left(\frac{\delta_n}{\delta_C}\right)\left(\frac{\delta_s}{\delta_C}\right) & -\frac{\sigma_C}{\delta_C(1-\lambda_{cr})}\left(\frac{1}{\lambda_e^3}\right)\left(\frac{\delta_n}{\delta_C}\right)\left(\frac{\delta_p}{\delta_C}\right) \\ -\frac{\sigma_C}{\delta_C(1-\lambda_{cr})}\left(\frac{1}{\lambda_e^3}\right)\left(\frac{\delta_s}{\delta_C}\right)\left(\frac{\delta_n}{\delta_C}\right) & -\frac{\sigma_C}{\delta_C(1-\lambda_{cr})}\left(1 - \frac{1}{\lambda_e} + \frac{1}{\lambda_e^3}\left(\frac{\delta_s}{\delta_C}\right)^2\right) & -\frac{\sigma_C}{\delta_C(1-\lambda_{cr})}\left(\frac{1}{\lambda_e^3}\right)\left(\frac{\delta_s}{\delta_C}\right)\left(\frac{\delta_p}{\delta_C}\right) \\ -\frac{\sigma_C}{\delta_C(1-\lambda_{cr})}\left(\frac{1}{\lambda_e^3}\right)\left(\frac{\delta_p}{\delta_C}\right)\left(\frac{\delta_n}{\delta_C}\right) & -\frac{\sigma_C}{\delta_C(1-\lambda_{cr})}\left(\frac{1}{\lambda_e^3}\right)\left(\frac{\delta_p}{\delta_C}\right)\left(\frac{\delta_s}{\delta_C}\right) & -\frac{\sigma_C}{\delta_C(1-\lambda_{cr})}\left(1 - \frac{1}{\lambda_e} + \frac{1}{\lambda_e^3}\left(\frac{\delta_p}{\delta_C}\right)^2\right) \end{bmatrix} \tag{9}$$

Finally in the unloading phase, the matrix C_f can be obtained from eq. (5) as

$$C_f = \begin{bmatrix} C_{nn} & C_{ns} & C_{np} \\ C_{sn} & C_{ss} & C_{sp} \\ C_{pn} & C_{ps} & C_{pp} \end{bmatrix}$$
$$= \begin{bmatrix} \frac{\sigma_C}{\delta_C}\left(\frac{1-\lambda_{max}}{1-\lambda_{cr}}\right)\frac{1}{\lambda_{max}} & 0 & 0 \\ 0 & \frac{\sigma_C}{\delta_C}\left(\frac{1-\lambda_{max}}{1-\lambda_{cr}}\right)\frac{1}{\lambda_{max}} & 0 \\ 0 & 0 & \frac{\sigma_C}{\delta_C}\left(\frac{1-\lambda_{max}}{1-\lambda_{cr}}\right)\frac{1}{\lambda_{max}} \end{bmatrix} \tag{10}$$

It must be noted that for the non-cohesive regions, the standard tangent modulus is employed in the stiffness matrix.

2.2. Finite element implementation

In order to derive the stiffness matrix of three-dimensional cohesive element, the bilinear cohesive model described in the preceding section is implemented in the framework of finite element method. The derivation of stiffness matrix of cohesive element is similar to the stiffness matrix of contact friction element, in which the contact constitutive relation must be replaced by the cohesive material matrix C_f given in relations (8)-(10). The cohesive element includes two surfaces with distinctive nodal points, which are initially coincident. The displacement field of the cohesive element may be linear, or higher order. Fig. 4 presents an eight-noded linear cohesive element. To obtain the stiffness matrix of cohesive element in global coordinate system, we need to relate the global displacement vector to the local separation vector. The vector of relative displacements between two homologous points can be obtained from the displacement fields associated to the element faces (top and bottom) as

$$\boldsymbol{\delta} = \mathbf{u}^{top} - \mathbf{u}^{bot} \tag{11}$$

where $\boldsymbol{\delta} = \langle\, \delta_n \quad \delta_s \quad \delta_p \,\rangle^T$ and $\mathbf{u} = \langle\, u_n \quad u_s \quad u_p \,\rangle^T$. A local co-ordinate system is established at a point on the cohesive element by obtaining the vector normal to the element surface using the cross-product of two vectors as
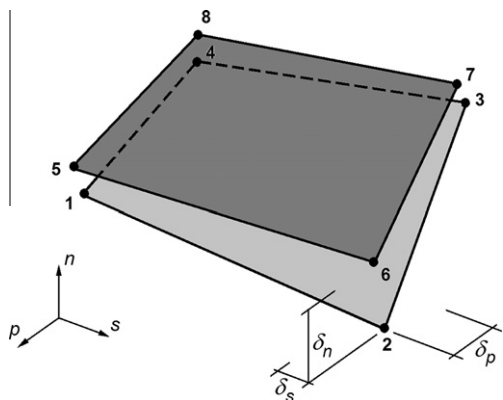

Fig. 4. An eight-noded cohesive element.

$$\mathbf{n} = \frac{1}{A}\left\{ \begin{array}{c} \frac{\partial x}{\partial \xi} \\ \frac{\partial y}{\partial \xi} \\ \frac{\partial z}{\partial \xi} \end{array} \right\} \times \left\{ \begin{array}{c} \frac{\partial x}{\partial \eta} \\ \frac{\partial y}{\partial \eta} \\ \frac{\partial z}{\partial \eta} \end{array} \right\} \tag{12}$$

where ξ and η are the natural coordinates in the plane of cohesive element, and A is the length of vector normal to the cohesive element surface that represents the unit mapped area of the plane of cohesive element. The derivatives in relation (12) are coefficients of the Jacobian matrix of the co-ordinate transformation. The two tangent vectors can be formed by $\mathbf{s} = \langle 1,0,0\rangle^T \times \mathbf{n}$ and $\mathbf{p} = \mathbf{s} \times \mathbf{n}$. If the direction of $\mathbf{n}$ is exactly in the x-direction then $\mathbf{s}$ can be obtained by $\mathbf{s} = \langle 0,1,0\rangle^T \times \mathbf{n}$.

The relative displacements of relation (11) can be therefore written using the standard iso-parametric shape functions of the cohesive element as

$$\boldsymbol{\delta} = \mathbf{R}^T(\mathbf{N}^{top}\bar{\mathbf{u}}^{top} - \mathbf{N}^{bot}\bar{\mathbf{u}}^{bot}) \tag{13}$$

or

$$\boldsymbol{\delta} = \mathbf{R}^T \{\, -\mathbf{N}^{bot} \quad \mathbf{N}^{top} \,\} \left\{ \begin{array}{c} \bar{\mathbf{u}}^{bot} \\ \bar{\mathbf{u}}^{top} \end{array} \right\} \equiv \mathbf{B}_f \bar{\mathbf{u}} \tag{14}$$

where $\mathbf{R} = \langle \mathbf{n}, \mathbf{s}, \mathbf{p} \rangle$ and $\mathbf{N}^{bot} = \mathbf{N}^{top} = \langle N_1\mathbf{I}, N_2\mathbf{I}, N_3\mathbf{I}, N_4\mathbf{I} \rangle$.

The stiffness matrix of three-dimensional cohesive fracture element can be therefore evaluated similar to the standard finite element manner, in which for the numerical integration of cohesive element, the integration over the domain can be replaced by the integration over the iso-parametric coordinates ξ and η as

$$\mathbf{K}_f = \int_{\xi=-1}^{\xi=+1} \int_{\eta=-1}^{\eta=+1} \mathbf{B}_f^T \mathbf{C}_f \mathbf{B}_f \det\mathbf{J}\, d\xi d\eta \tag{15}$$

where $\det\mathbf{J}$ denotes the determinant of the Jacobian matrix. The cohesive material matrix $\mathbf{C}_f$ is defined in relations (8)-(10). For the linear eight-noded cohesive element, the stiffness matrix is a 24×24 matrix corresponding to the three degrees-of-freedom defined at each nodal point.

3. Crack propagation criteria

There are basically two types of crack tips in the crack growth of cohesive fracture mechanics; the real crack tip and the fictitious crack tip. The real crack tip is the point that separates the stress free zone from the cohesive stress zone, while the fictitious crack tip is the point that separates the cohesive zone from the uncracked zone. In two-dimensional fracture mechanics, the crack surface may be straight or curved, however – in three-dimensional crack growth, the crack surface may be straight, curved, planar, or non-planar. Hence, the fracture behavior associated with three-dimensional crack growth depends on both the crack front curvature and the crack surface curvature. There are various numerical techniques proposed in the literature for tracking the 3D non-planar crack path. The level set method is a numerical approach in modeling the motion of interfaces that was recently adopted by Moës et al. (2002) to model the 3D crack propagation. The method uses the signed distance function to describe the crack-tip and crack surfaces. In this technique, two advance vectors are defined
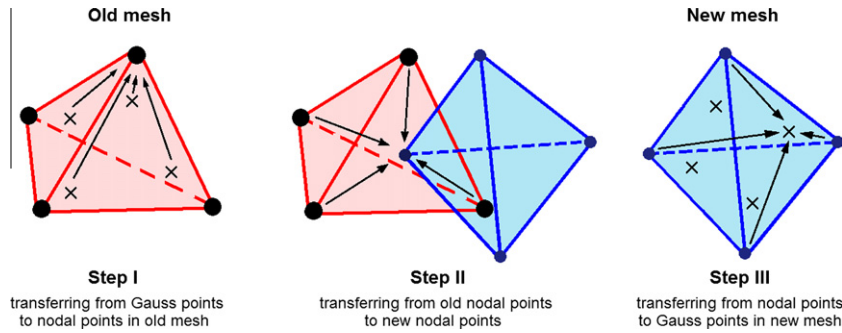
Fig. 5. Three-steps procedure of data transferring operator; ● nodal point, × Gauss points.
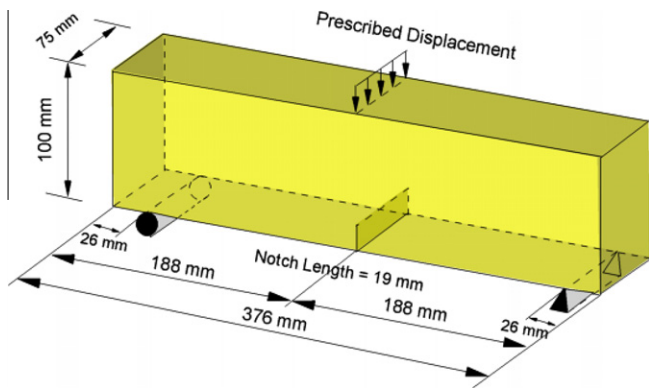

Fig. 6. The 3PB specimen with symmetric edge crack. The geometry and boundary conditions.

on the basis of failure criterion to determine the new position of the crack-tip. A global tracking algorithm was proposed by Oliver et al. (2004) for tracking 3D cracks, in which the discontinuity path inside the finite element was implemented at a pure element level. Gasser and Holzapfel (2006) proposed a local algorithm which is characterized by recursively cutting elements using a two-step algorithm for tracking 3D crack paths.

In this study, a direct criterion is employed based on the maximal principal stress, originally proposed by Bouchard et al. (2003), to validate the technique in 3D non-planar crack growth. In this criterion, the maximum principal stresses and their axes are evaluated at the nearest integration points to the crack tip. The direction of crack propagation is perpendicular to the vector obtained by the weighted average of each direction with respect to the distance between the integration point and the crack tip. In 3D crack growth, this vector is not unique and is constructed on the basis of two other principal directions. The target vector is the weighted combination of two principal vectors corresponding to the minimum and mid-stresses. The weighting parameter of each vector can be obtained according to the corresponding principal stress. Consider the maximum, minimum and mid-stresses are represented by σ_{max}, σ_{min} and σ_{mid}, respectively, and their corresponding principal vectors by $\mathbf{u}_1$, $\mathbf{u}_2$ and $\mathbf{u}_3$, the propagation vector can be defined as

$$\mathbf{v} = \sigma_{min}\mathbf{u}_2 + \sigma_{mid}\mathbf{u}_3 \tag{16}$$

The above vector determines the direction of crack propagation at each step, however – the length of crack growth depends on the desired accuracy of simulation at each increment, and can be assumed as a small value if the kinking of the crack has a large value. The propagation vector must be determined at each nodal point of the crack front. This vector can be used to connect the old fictitious

crack tip to the new fictitious crack tip in order to construct the new crack front. The space between the old and new crack fronts is then modeled by the cohesive fracture elements. It must be noted that this algorithm results in the fictitious crack tip where the cohesive zone is separated from the uncracked zone and the real crack tip moves when the relative displacement exceeds the critical displacement δ_C.

4. Error estimation and adaptive remeshing

The accuracy in numerical analysis of finite element solution strongly depends on the quality of FE mesh. In crack growth simulation, the mesh refinement takes an important role to capture the local parameters accurately where the stress concentration occurs. The objective of adaptive technique is to obtain a mesh which is optimal in the sense that the computational costs are minimal under the constraints, and the error of finite element solution is acceptable within a certain limit. In addition, the remeshing procedure ensures that the new boundary and resulting discontinuity is taken into account properly in the represented model independent of previous discretization. Since the exact solution of state variables is not available, the recovered solution can be used instead of the exact solution and approximate the error as the difference between the recovered values and those obtained directly from the finite element solution. In order to obtain an improved solution, the nodal smoothing procedure is performed using the weighted superconvergent patch recovery (WSPR) technique, proposed by Moslemi and Khoei (2009) to simulate the crack growth in cohesive fracture zone. The concept of superconvergence is that, at some points, the rate of convergence is higher than those of other points. Zienkiewicz and Zhu (1992) presented that the Gauss integration points of isoparametric elements are superconvergent. In WSPR technique, it is assumed that the nodal values belong to a polynomial expansion of the same complete order p, which is valid over an element patch surrounding the particular assembly node. Thus, the recovered stress can be obtained as a polynomial with unknown coefficients for each component as

$$\sigma_i^* = a_0 + a_1 x + a_2 y + a_3 z + \cdots + a_n z^n$$
$$= \langle 1, x, y, z, \ldots, z^n \rangle \langle a_0, a_1, a_2, a_3, \ldots, a_n \rangle^T = \mathbf{Pa} \tag{17}$$

where $\mathbf{P}$ contains the appropriate polynomial terms and $\mathbf{a}$ is a set of unknown parameters. The unknown vector $\mathbf{a}$ can be determined by performing a least square fit of σ_i^* to the existing data of finite element solution at the Gauss quadrature points of elements patch for considered vertex node. In the WSPR technique, the weighting parameters are assumed for the sampling points of the patch, which results in more realistic recovered values at the nodal points, particularly near the crack tip and boundaries. Hence, if we have n sampling points in the patch with the coordinates (x_k, y_k, z_k) the error function F can be written as
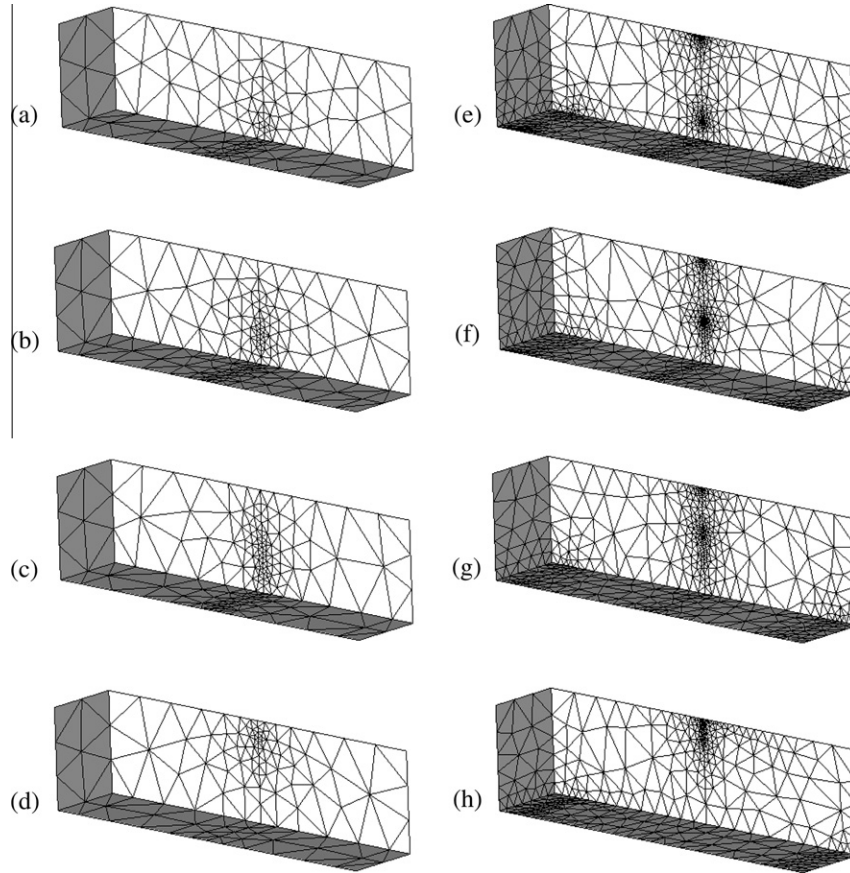
Fig. 7. Adaptive mesh refinements in 3PB specimen with symmetric edge crack at different loading steps; (a–d) Initial uniform meshes, (e–h) adapted meshes.
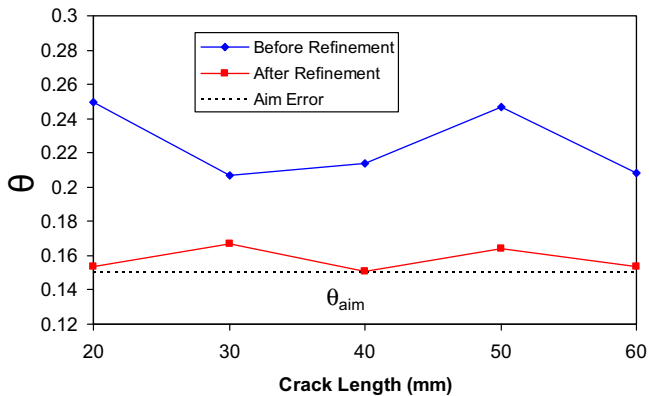

Fig. 8. The variation of estimated error with crack length during adaptive remeshing in 3PB specimen with symmetric edge crack.

$$F(\mathbf{a}) = \sum_{k=1}^{n} w_k [\sigma_i^*(x_k, y_k, z_k) - \hat{\sigma}_i(x_k, y_k, z_k)]^2$$

$$= \sum_{k=1}^{n} w_k [\mathbf{P}(x_k, y_k, z_k)\mathbf{a} - \hat{\sigma}_i(x_k, y_k, z_k)]^2 \qquad (18)$$

where $\hat{\sigma}_i$ is the stress component derived by the finite element solution at each Gauss quadrature point of the patch and n is the number of sampling points. In above relation, w_k denotes the weighting parameter at each sampling point which reflects the effect of distance between the recovered nodal point and the sampling point. Thus, we define the weighting parameter $w_k = 1/r_k$, with r_k denoting

the distance of each sampling point from the vertex node which is under recovery. Minimizing the error function $F(\mathbf{a})$ results in

$$\mathbf{a} = \left(\sum_{k=1}^{n} w_k^2 \mathbf{P}_k^T \mathbf{P}_k \right)^{-1} \sum_{k=1}^{n} w_k^2 \mathbf{P}_k^T \hat{\sigma}_i(x_k, y_k, z_k) \qquad (19)$$

Based on above procedure, the recovered values σ_i^* can be obtained at each nodal point. The error can be therefore approximated by $\mathbf{e}_\sigma \approx \mathbf{e}_\sigma^* = \boldsymbol{\sigma}^* - \hat{\boldsymbol{\sigma}}$, in which $\mathbf{e}_\sigma$ denotes the exact error and $\mathbf{e}_\sigma^*$ indicates the estimated error. Since the pointwise error becomes locally infinite in critical points, such as point load, the error estimator can be replaced by a global parameter using the L_2 norm of error defined as

$$\|\mathbf{e}_\sigma\| = \|\boldsymbol{\sigma}^* - \hat{\boldsymbol{\sigma}}\| = \left(\int_\Omega (\boldsymbol{\sigma}^* - \hat{\boldsymbol{\sigma}})^T (\boldsymbol{\sigma}^* - \hat{\boldsymbol{\sigma}}) d\Omega \right)^{\frac{1}{2}} \qquad (20)$$

4.1. Adaptive mesh refinement

In adaptive mesh refinement, the L_2 norm of each element is a more desirable quantity to optimize the mesh. The global error norm can be achieved by using the sum square root of elements error norm, i.e. $\|\mathbf{e}_\sigma\|^2 = \sum_{i=1}^{m} \|\mathbf{e}_\sigma\|_i^2$, with i denoting the element contribution and m the total number of elements. In order to normalize the value of error norm, the L_2 norm is divided to the state variable, such as the stress norm. Thus, the overall percentage error can be defined by $\theta = \|\mathbf{e}_\sigma\|/\|\hat{\boldsymbol{\sigma}}\|$. This relative error norm can be used in the mesh refinement procedure. Since the total error permissible must be less than a certain value, it is a simple matter to search the design field for a new solution in which the total error satisfies this requirement. In fact, after remeshing each element
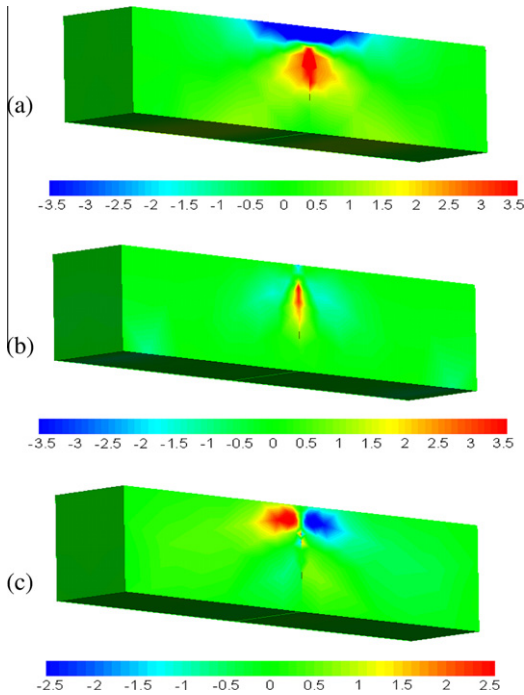
Fig. 9. The contours of stress distribution in 3PB specimen at the final loading step; (a) stress σ_x, (b) stress σ_y, (c) stress τ_{xy} (all dimensions in MPa).
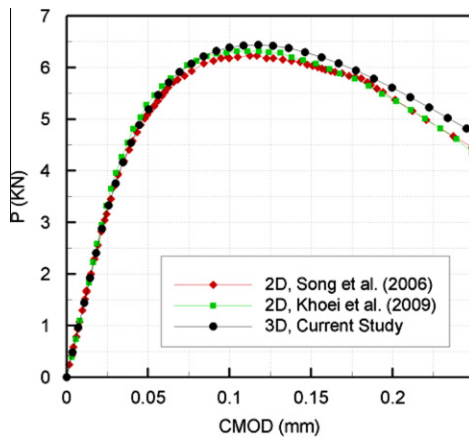

Fig. 10. The variations of vertical reaction with CMOD in 3PB specimen with symmetric edge crack.
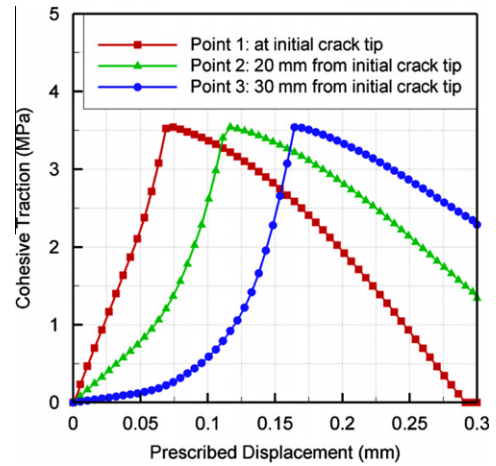

Fig. 11. The variation of cohesive traction with prescribed displacement at different points from the initial crack tip.
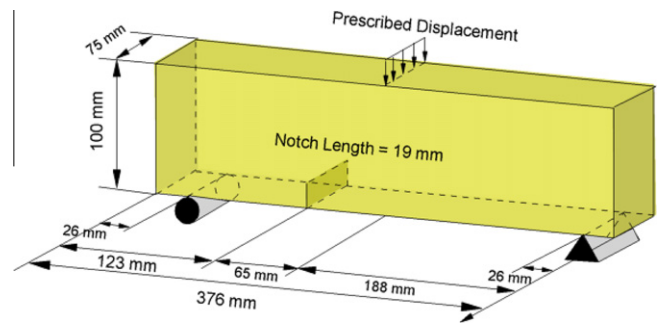

Fig. 12. The 3PB specimen with an eccentric crack; geometry and boundary conditions.
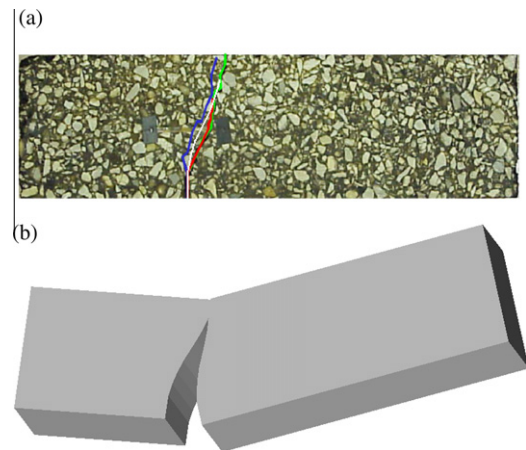

Fig. 13. The 3PB specimen with an eccentric crack; (a) A comparison between the crack trajectory obtained by the proposed computational model (white) and those of experimental and numerical results (blue, green and red) reported by Song et al. (2006).

must obtain the same error and the overall percentage error must be less than the target percentage error, i.e.

$$\theta \leqslant \theta_{\text{aim}} = \frac{\|\mathbf{e}_\sigma\|_{\text{aim}}}{|\hat{\boldsymbol{\sigma}}\|} \tag{21}$$

The size of elements in the new mesh depends on the relative error and the rate of convergence. The rate of convergence of standard elements is proportional to the order of shape functions. In the case of singular problem, such as the linear fracture analysis (LEFM), it is proportional to the order of singularity. However, in the cohesive fracture analysis, the stress field is not singular and the rate of convergence is proportional to the order of shape functions. Thus, if h represents the size of element and λ denotes the rate of convergence, the new element size can be obtained as

$$(h_i)_{\text{new}} = \left[\frac{(\|\mathbf{e}_\sigma\|_i)_{\text{aim}}}{(\|\mathbf{e}_\sigma\|_i)_{\text{old}}}\right]^{1/\lambda} (h_i)_{\text{old}} \tag{22}$$

After indicating the size of elements from Eq. (21), a mesh satisfying the requirements will be finally generated by an efficient mesh generator which allows the new mesh to be constructed according to a predetermined size. In order to prevent the mesh generation difficulties due to very small and large elements, the element size is limited by an upper and a lower bound, i.e. $\bar{h}_{\text{min}} \leqslant (h_i)_{\text{new}} \leqslant \bar{h}_{\text{max}}$. The cohesive surfaces would be preserved
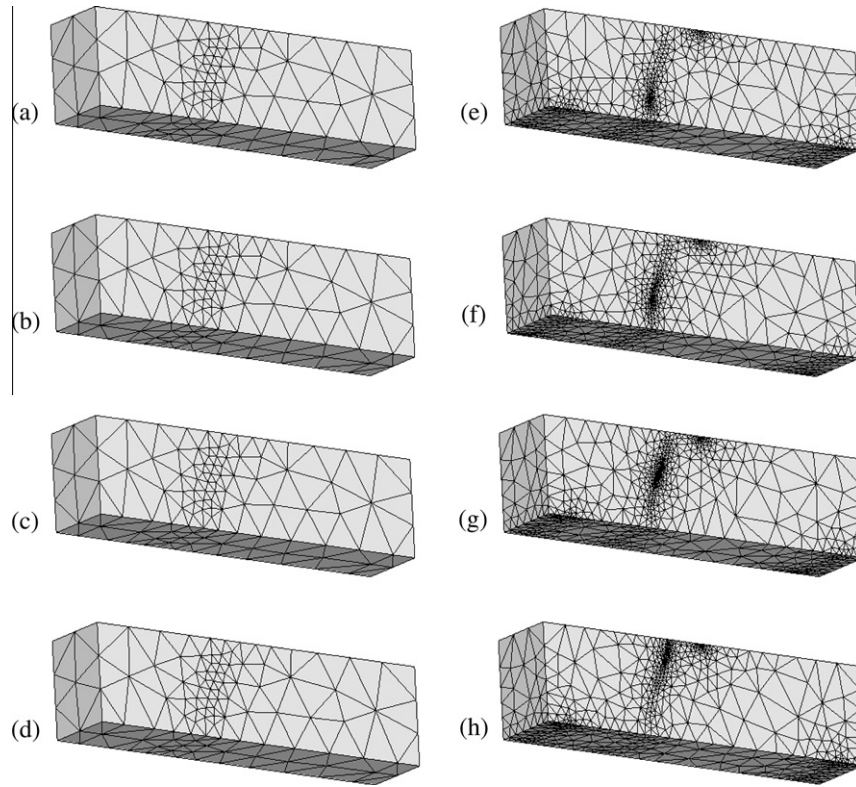
Fig. 14. Adaptive mesh refinements in 3PB specimen with an eccentric crack at different loading steps; (a–d) initial uniform meshes, (e–h) adapted meshes.
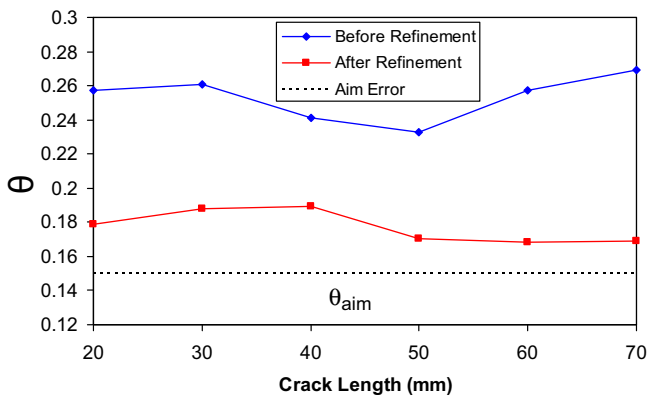

Fig. 15. The variation of estimated error with crack length during adaptive mesh refinement in 3PB specimen with an eccentric crack.

Fig. 16. The variations of vertical reaction with CMOD in 3PB specimen with an eccentric crack.

in the geometry of problem by two concordant surfaces, and the new cohesive elements would be adjusted to these surfaces according to the mesh density. In the nonlinear FE analysis, such as cohesive zone model, the new mesh must be used starting from the end of previous load step since the solution is history-dependent in nonlinear problems. Thus, the state and internal variables need to be mapped from the old finite element mesh to the new one. The data transfer between the old and new meshes is one of the most challenging parts of nonlinear analysis. It is important that the transfer of information from the old to new meshes is achieved with minimum discrepancy in equilibrium and constitutive relations (Khoei et al., 2007). It must be noted that the data transfer operator would produce some numerical diffusions, however – it was shown by Zienkiewicz and Zhu (1992) that the implementation of the superconvergant points minimizes this numerical
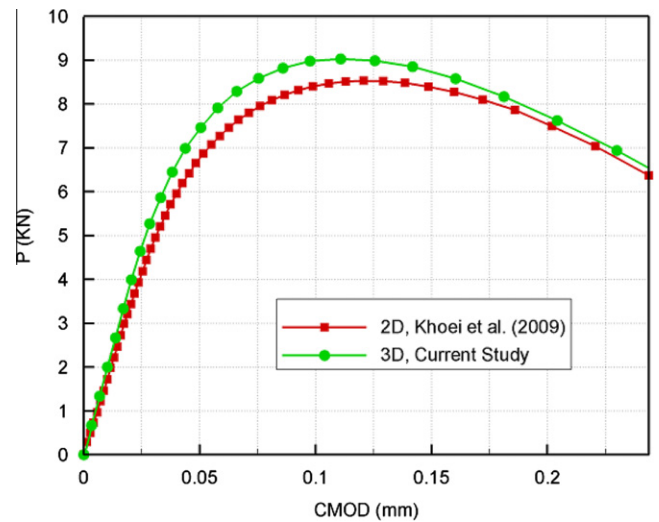
diffusion. In the present study, the data transfer operators developed by Gharehbaghi and Khoei (2008) and Khoei and Gharehbaghi (2009) in 3D large plasticity deformations is applied based on the superconvergent patch recovery (SPR) technique.

4.2. Data transfer operator

In order to map the state and internal variables from the old finite element mesh to the new one, the process of data transfer is carried out in three steps. Consider that a state array $\Lambda_n^{\text{old}} = (\mathbf{u}_n^{\text{old}}, \varepsilon_n^{\text{old}}, \sigma_n^{\text{old}})$ denote the values of displacement, strain ten-
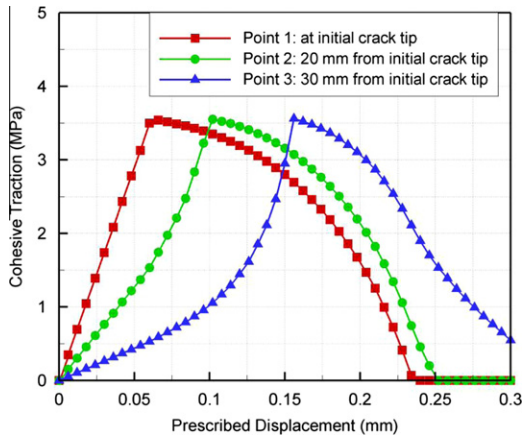
Fig. 17. The variation of cohesive traction with prescribed displacement at different points from the initial crack tip.
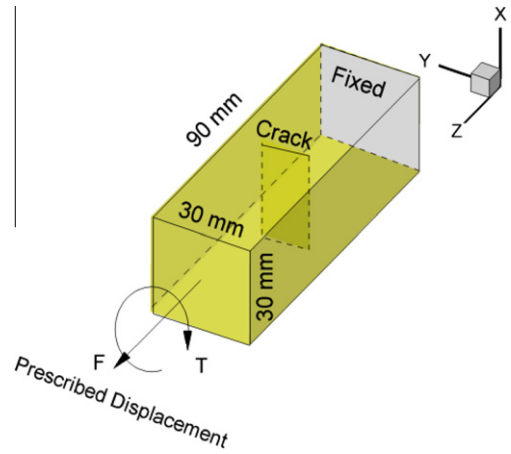

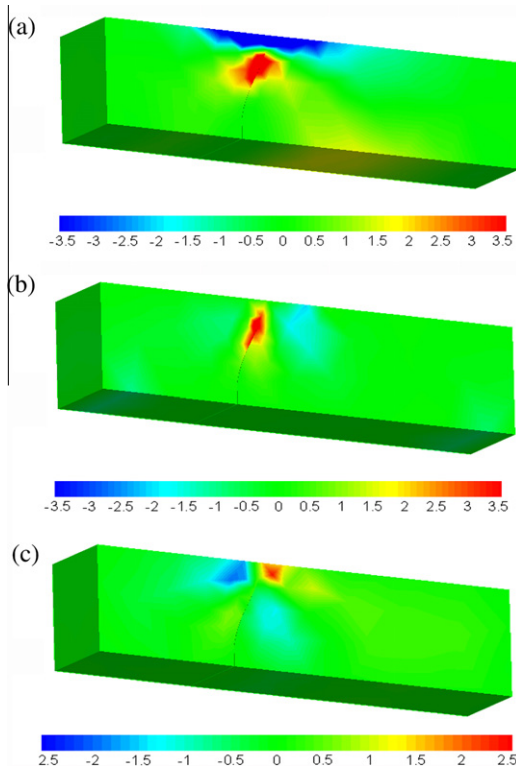**Fig. 19.** The tension–torsion specimen with center through crack. The geometry and boundary conditions.

$$(\boldsymbol{\sigma}_n)_G^{\text{new}} = T_1 [(\boldsymbol{\sigma}_n)_G^{\text{old}}] \tag{23}$$

The variables $(\boldsymbol{\sigma}_n)_G^{\text{old}}$ specified at Gauss points of the mesh M_h are transferred by the operator T_1 to each point of the domain Ω, in order to specify the variables $(\boldsymbol{\sigma}_n)_G^{\text{new}}$ at the Gauss points of new mesh M_H. The operator T_1 can be constructed by a suitable projection technique, such as the superconvergent patch recovery method.

In order to obtain the continuous values of stress tensor $(\boldsymbol{\sigma}_n)^{\text{old}}$, the Gauss point components $(\boldsymbol{\sigma}_n)_G^{\text{old}}$ are projected to nodal points to evaluate the components $(\boldsymbol{\sigma}_n)_N^{\text{old}}$. In this study, the projection of the Gauss point components to the nodal points is carried out using the weighted-SPR technique, as described in previous section. The nodal components of the stress tensor $(\boldsymbol{\sigma}_n)_N^{\text{old}}$ for the mesh M_h are then transferred to the nodes of the new mesh M_H resulting in components $(\boldsymbol{\sigma}_n)_N^{\text{new}}$. The components of stress tensor at the Gauss points of the new mesh M_H, i.e. $(\boldsymbol{\sigma}_n)_G^{\text{new}}$ are finally obtained by using the interpolation of the shape functions of the new finite elements. In this procedure, the local coordinates are used to interpolate the variables from the nodes of mesh M_h to the nodes of mesh M_H. The three steps of the data transfer procedure are illustrated schematically in Fig. 5.

5. Numerical simulation results

In order to illustrate the accuracy and efficiency of proposed adaptive mesh strategy in the three-dimensional cohesive crack model described in preceding sections, several practical examples are analyzed numerically. Two benchmark examples are chosen to evaluate the performance of adaptive FE strategy for the cohesive crack growth in a bending beam with symmetric and eccentric edge cracks. The next two examples include the 3D crack growth with complex geometries, in which the crack growth produces the non-planar curved crack front and crack surfaces. The ten-noded tetrahedral elements are employed for the finite element meshes together with the four Gauss–Legendre quadrature points for the numerical integration. The eight-noded cohesive elements are applied for the cohesive fracture zone in successive crack growth steps. In all numerical examples, the behavior of bulk material is assumed to be the linear elastic. In the simulation of crack growth and evaluation of cohesive tractions, the maximum principal stress criterion is employed to determine the crack growth direction. In addition, various uniform and adaptive mesh refinements are implemented to evaluate the estimated error and

Fig. 18. The contours of stress distribution in 3PB specimen with an eccentric crack at the final loading step; (a) stress σ_x, (b) stress σ_y, (c) stress τ_{xy} (all dimensions in MPa).

sor and stress tensor at time t_n for the mesh M_h. Also assume that the estimated error of the solution Λ_n^{old} respects the prescribed criteria, while these are violated by the solution $\Lambda_{n+1}^{\text{old}}$. In this case, a new mesh M_H is generated and a new solution $\Lambda_{n+1}^{\text{new}}$ is computed by evaluating the stress tensor $\boldsymbol{\sigma}_n^{\text{new}}$ for a new mesh M_H at time step t_n. In this way, the state array $\hat{\Lambda}_n^{\text{new}} = (\mathbf{u}_n^{\text{new}}, \boldsymbol{\sigma}_n^{\text{new}})$ is constructed, where $\hat{\Lambda}$ is used to denote a reduced state array. It must be noted that the state array $\hat{\Lambda}$ characterizes the history of the material and provides sufficient information for computation of a new solution $\Lambda_{n+1}^{\text{new}}$. The aim is to transfer the internal variables $(\boldsymbol{\sigma}_n)_G^{\text{old}}$ stored at the Gauss points of the old mesh M_h to the Gauss points of new mesh M_H. The transfer operator T_1 between meshes M_h and M_H can be defined as
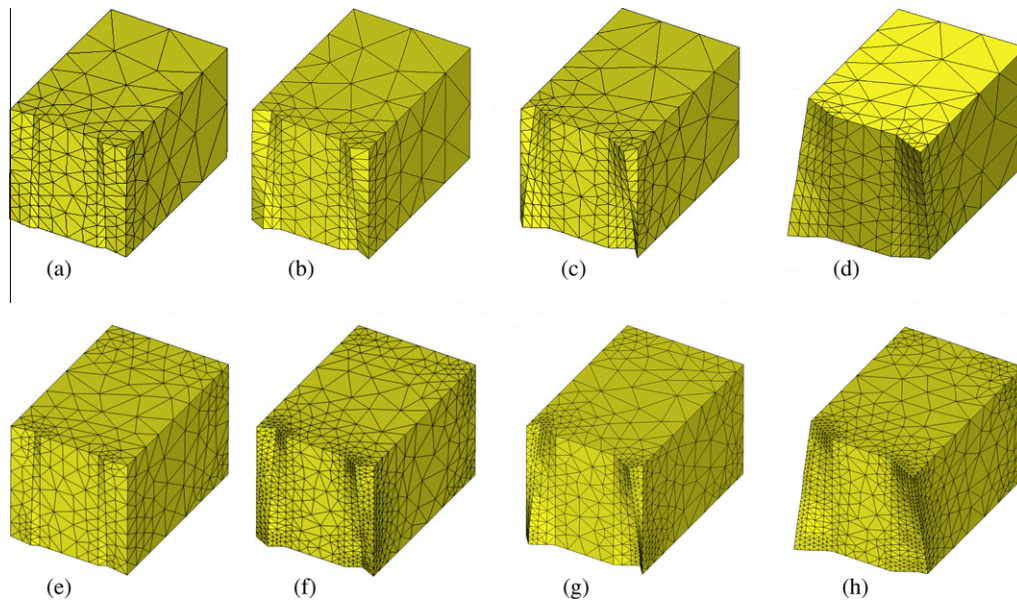
Fig. 20. Adaptive mesh refinements in the tension–torsion specimen with center through crack at different loading steps; (a–d) initial uniform meshes, (e–h) adapted meshes.

Table 1
The number of elements and nodal points of initial and adapted meshes in the tension–torsion specimen with center through crack at various steps.

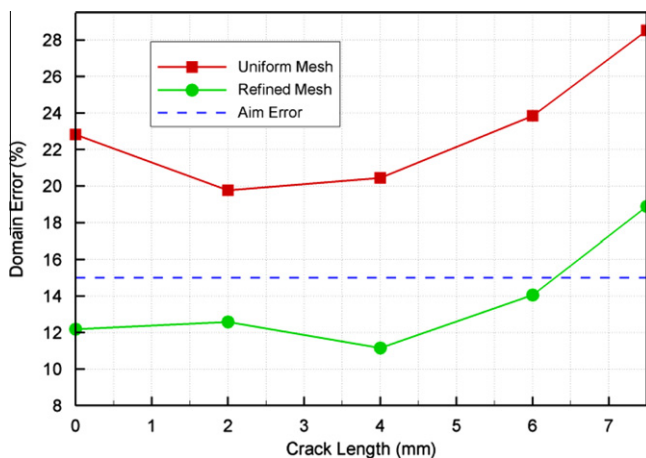| Loading step	Uniform mesh		Refined mesh	
	Number of nodes	Number of elements	Number of nodes	Number of elements
Step 1	767	361	6034	3642
Step 2	2523	1354	9598	5926
Step 3	2836	1528	23482	14856
Step 4	3316	1725	17139	10740
Step 5	3344	1818	25214	15723

Fig. 21. The variation of estimated error with crack length during adaptive mesh refinement in the tension–torsion specimen with center through crack.

mesh refinement procedure. In all examples, the results are compared with those reported in literature.

5.1. Three point bending beam with symmetric edge crack

In the first example, a simply supported beam with an edge notch at the mid plane is numerically analyzed. This example is chosen to demonstrate the performance of proposed adaptive strategy together with the cohesive zone model for a benchmark

problem. The beam is constructed using the asphalt concrete and has a vertical edge crack, as shown in Fig. 6. The beam has the length of 376 mm, height of 100 mm and thickness of 75 mm. The initial notch is 19 mm at the center of bottom edge of the beam. A prescribed displacement is gradually exerted to the center of top edge of the beam until the failure of the beam happens. The material properties of the beam and the cohesive zone parameters are chosen as follows; E = 14.2 GPa, v = 0.35, σ_c = 3.56 MPa and G_c = 344 J/m^2. The value of non-dimensional critical displacement is chosen as $\lambda_{cr} = 0.04$. This specimen was simulated by Song et al. (2006) and Khoei et al. (2009) using the 2D FE modeling to validate the performance of their cohesive model.

The adaptive mesh refinement process is carried out in this example using the weighted SPR technique for the target error of 15%. In Fig. 7, the successive mesh refinements are shown during the crack growth simulation at different loading steps using the uniform and adapted mesh refinements. As can be expected, the crack grows symmetrically until the ultimate failure of the beam. Obviously, the cohesive behavior near the fictitious crack zone results in the high value of estimated error, and consequently a very dense mesh is produced at this region. In Fig. 8, the variation of error estimator θ is shown for the uniform and adapted meshes. Clearly, the adaptive mesh refinements result in a uniform estimated error and converge to the prescribed target error. In Fig. 9, the contours of stress distribution σ_x, σ_y and τ_{xy} are presented at the final loading step. The effect of cohesive tractions at the crack edges is obvious in these contours. The variation of vertical reaction is plotted with crack mouth opening displacement (CMOD) in Fig. 10. It shows a good agreement between the predicted
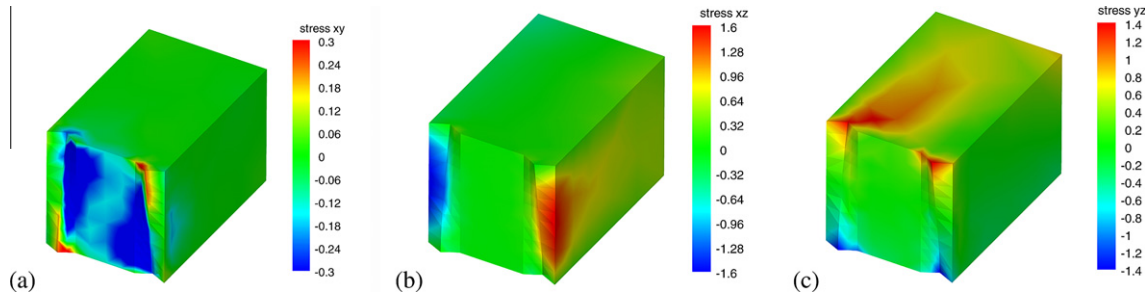
Fig. 22. The contours of stress distribution at final step of loading in the tension–torsion specimen; (a) stress τ_{xy}, (b) stress τ_{xz}, (c) stress τ_{yz} (all dimensions in MPa).

Fig. 24. The variations of total cohesive traction with crack opening at different points from the initial crack tip in the tension–torsion specimen.
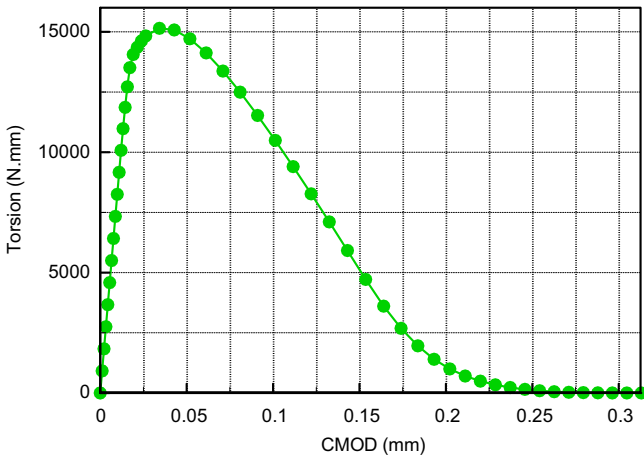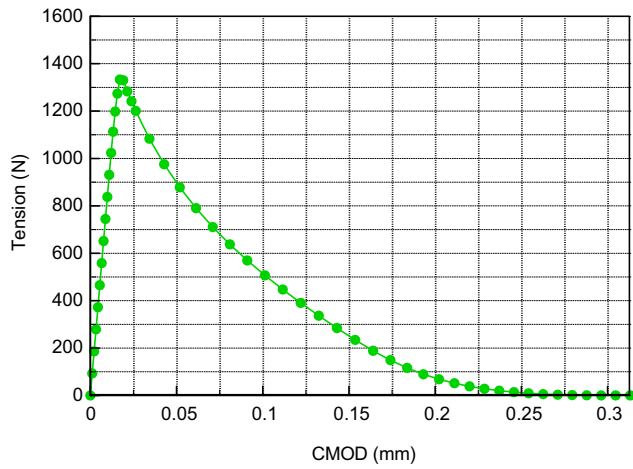

Fig. 23. The variations of tensile and torsion reactions with initial crack tip opening in the tension–torsion specimen with center through crack.

Fig. 25. The inclined penny-shaped crack; problem definition.

simulation and those reported by Song et al. (2006) and Khoei et al. (2009) using 2D FE modeling. Fig. 11 presents the variation of cohesive traction with prescribed displacement at different points from the initial crack tip. The consecutive curves imply the gradual movement of softening zone in the model.

5.2. Three point bending beam with an eccentric crack

In the second example, the 3D cohesive crack simulation is performed for the beam of previous example, in which the crack is considered at 65 mm from the center of the beam. The geometry and boundary conditions of the beam are given in Fig. 12. In contrast to the first example, the mixed mode crack propagation is
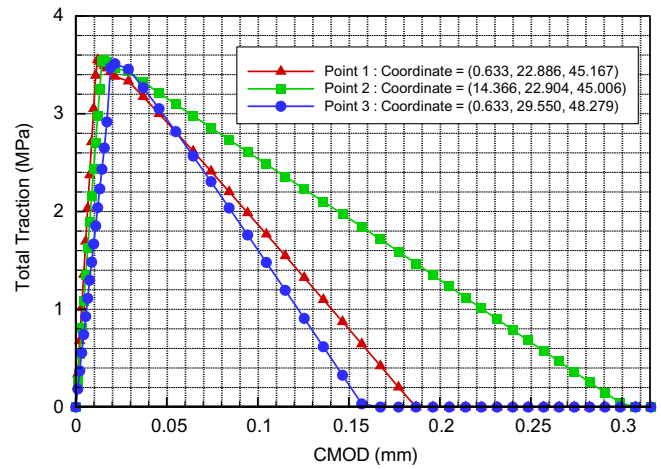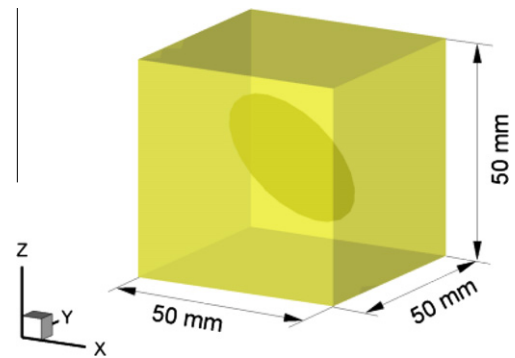
activated in this example and the crack kinking occurs. The material properties of the beam and the cohesive parameters are similar to the previous example. This beam was simulated by Song et al. (2006) using the 2D FE modeling, and was shown that the crack propagates to the center of the beam. In Fig. 13, the crack trajectory is shown together with the deformed shape of the beam using the proposed 3D computational model. A comparison of crack trajectory can be observed between the current simulation and those of experimental and numerical results reported by Song et al. (2006). The successive mesh refinements are performed during the crack propagation process, as shown in Fig. 14. In this figure, the initial and refined meshes are shown at various loading steps. As can be expected, the cohesive zone is refined with dense mesh to capture the high stress gradients at this region. The variation of
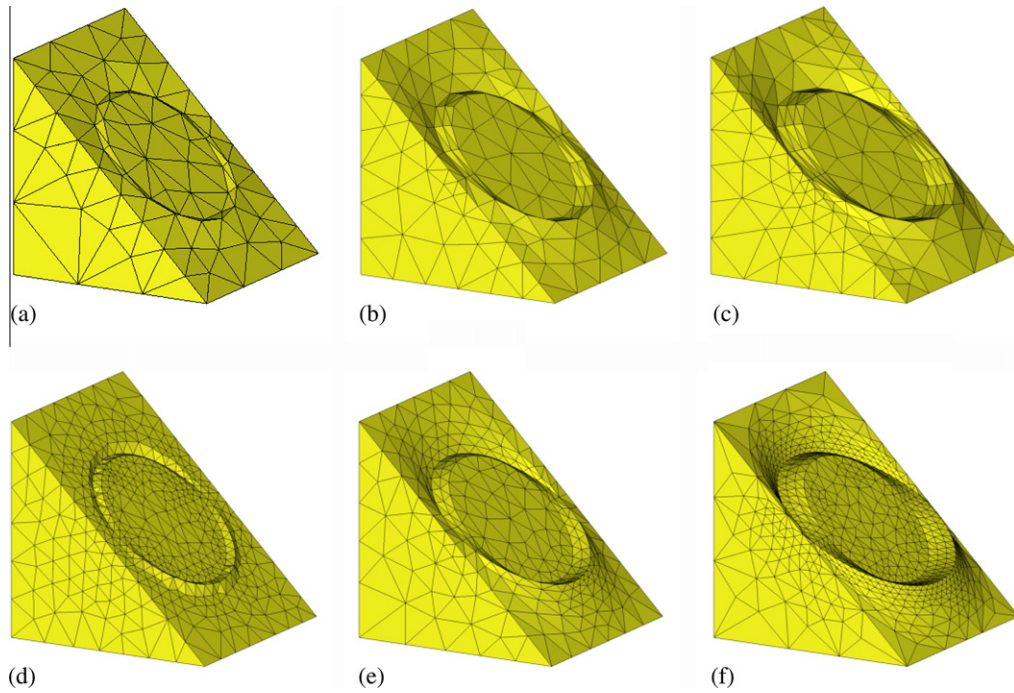
Fig. 26. Adaptive mesh refinements in the inclined penny-shaped crack at different loading steps; (a–c) initial uniform meshes, (d–f) adapted meshes.
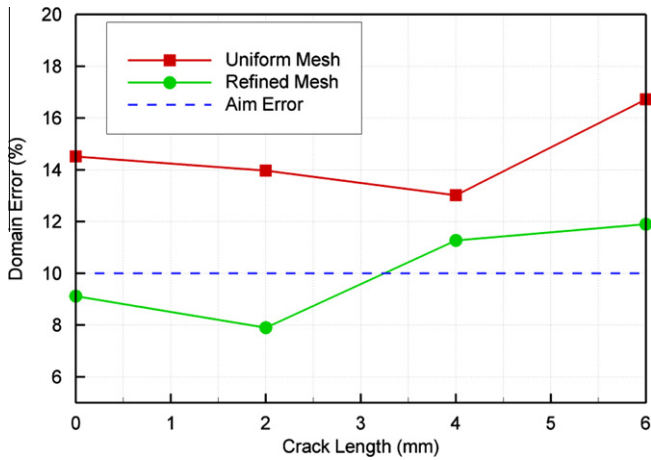

Fig. 27. The variation of estimated error with crack length during adaptive mesh refinement in the inclined penny-shaped crack.

error estimator θ with crack length is shown in Fig. 15 for the uniform and adapted meshes. The effect of adaptive mesh refinements at different crack lengths is obvious in this figure.

In Fig. 16, the variation of vertical reaction with CMOD is compared with that obtained for 2D crack propagation by Khoei et al. (2009). A little discrepancy observed in this figure can be justified by the fact that in 3D crack simulation, the nodes of cohesive elements along the thickness may undergo various separations. In Fig. 17, the variations of cohesive traction with prescribed

displacement are plotted at different points from the initial crack tip. Obviously, the cohesive forces increase during the crack propagation at the crack tip, and then decrease due to the softening behavior. A comparison between Figs. 11 and 17 presents that the cohesive elements in the current example are collapsed at earlier stages, which is because of the contribution of shear separation in cohesive elements. Finally, the contours of stress distribution σ_x, σ_y and τ_{xy} are shown in Fig. 18 at the final loading step. Different cohesive fracture behaviors can be observed in this figure; the cohesive elements above the crack tip display the linear behavior, the cohesive elements around the crack tip represent the softening behavior, and the cohesive elements below the crack tip are completely separated and present the zero stress values.

5.3. The tension–torsion specimen with center through crack

The next example is of a rectangular beam with center through crack, which is simultaneously subjected to the tension and torsion loadings. This example is chosen to demonstrate the effectiveness, robustness and accuracy of computational algorithm in the complex 3D non-planar crack propagation. The length of the beam is 90 mm and its cross section is a 30 mm square. There is a pre-existent through crack at the mid-span of the beam with 15 cm width. The beam is fixed at one end and subjected to the torsion and tension at the other end by applying the prescribed displacements. The geometry and boundary conditions of the problem are shown in Fig. 19. This example was modeled by Krysl and Belytschko

Table 2
The number of elements and nodal points of initial and adapted meshes in the inclined penny-shaped crack at various steps.

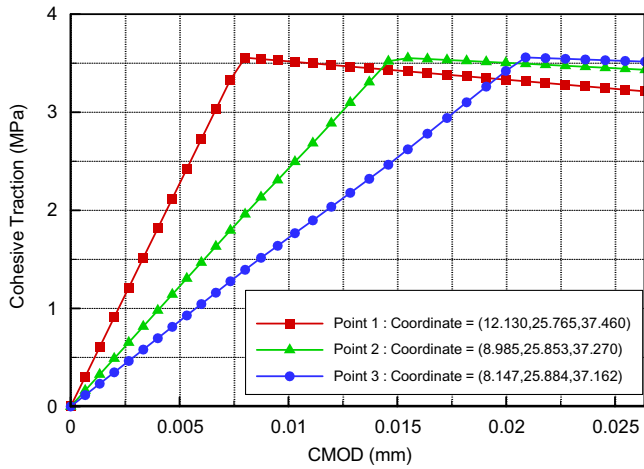| Loading step	Uniform mesh		Refined mesh	
	Number of nodes	Number of elements	Number of nodes	Number of elements
Step 0	540	294	12912	8781
Step 1	1432	890	21697	14979
Step 2	2638	1611	7566	4970
Step 3	3611	2269	24371	16847

Fig. 28. The variations of cohesive traction with crack opening at different points from the initial crack tip in the inclined penny-shaped crack.

(1999) using the element-free Galerkin method coupled with the standard finite element method.

In Fig. 20, the trajectory of crack propagation is depicted at different loading steps using the uniform and adaptive mesh refinements. These results demonstrate that there is a good agreement between the predicted crack path using the proposed computational algorithm and those reported by Krysl and Belytschko (1999). The properties of various mesh refinements are given in Table 1 for various loading steps. In Fig. 21, the effect of adaptive strategy can be observed on the estimated error at different crack growth. Obviously, the adaptive mesh refinements result in a reduced estimated error and converge to the prescribed target error. In Fig. 22, the contours of stress distribution τ_{xy}, τ_{yz} and τ_{zx} are presented at the final loading step. It has been observed that the tension is dominant in this example, and the torsion displays the shear cohesive tractions. The variations of tensile and torsion reactions with the initial crack tip opening are plotted in Fig. 23. Also plotted in Fig. 24 are the variations of total cohesive traction with prescribed displacement at various points from the initial crack tip.
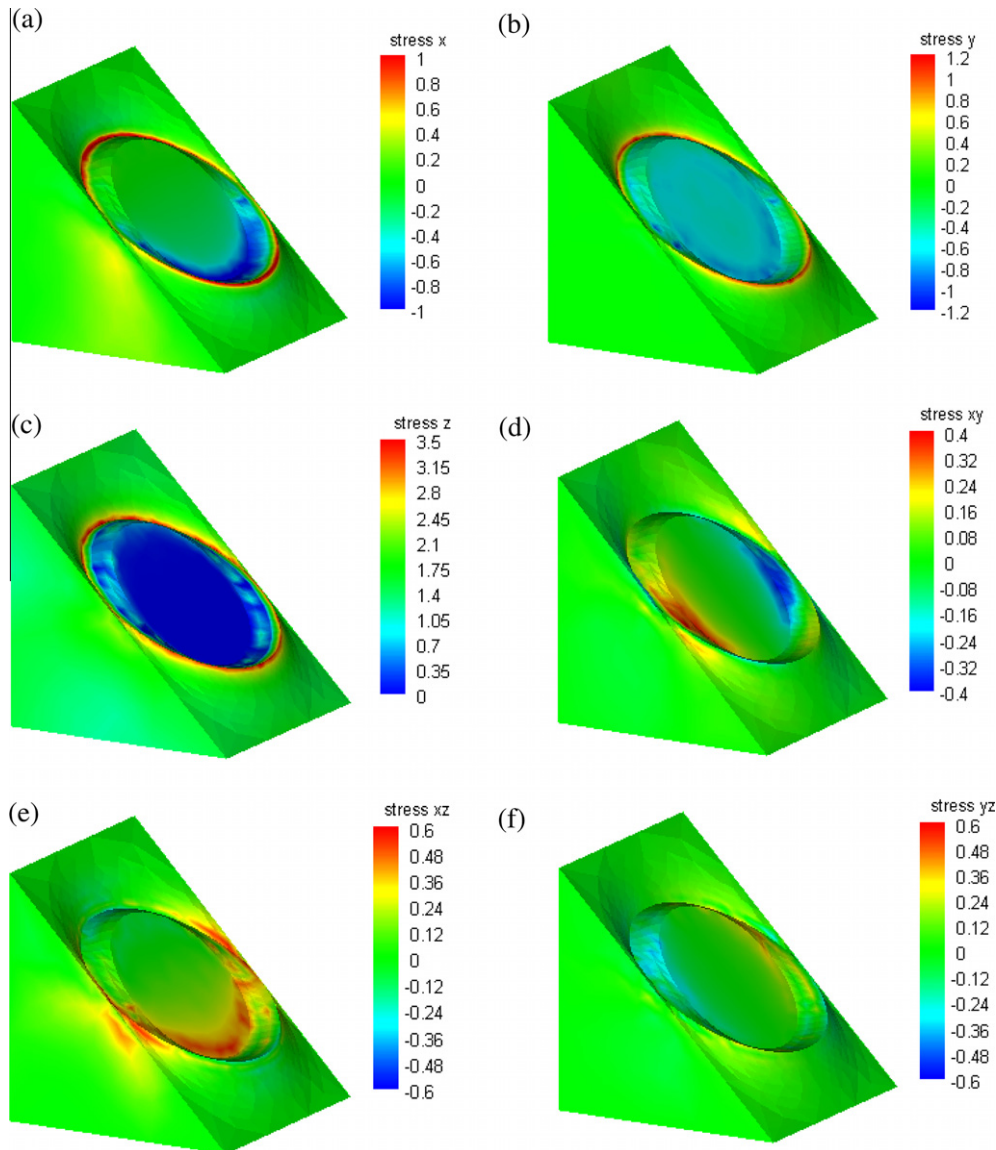

Fig. 29. The contours of stress distribution at final step of loading in the inclined penny-shaped crack; (a) stress σ_x, (b) stress σ_y, (c) stress σ_z, (d) stress τ_{xy}, (e) stress τ_{xz}, (f) stress τ_{yz} (all dimensions in MPa).

5.4. Inclined penny-shaped crack

The last example consists of an inclined penny-shaped crack in a cube with the dimension of 50 mm. The cube is subjected to a uniform tensile prescribed displacement along the top and bottom surfaces. The initial crack has a radius of 18 mm, which is located at the center of cube by the angle of 45° with the vertical axis, as shown in Fig. 25. This example illustrates the mixed-mode crack propagation, in which all three modes can be observed. In order to control the error of the solution, the adaptive FE mesh refinement is carried out to generate the optimal mesh at various loading steps. The weighted superconvergent patch recovery technique is used with the aim error of 10%. In Fig. 26, the successive mesh refinements are shown during the crack growth simulation at different loading steps using the uniform and adaptive mesh analyses for one-half of the specimen. The adaptive mesh refinement procedure reduces the estimated error considerably, as shown in Fig. 27. The number of elements and noded of uniform and adapted meshes are given in Table 2. Fig. 28 presents the variation of cohesive traction with prescribed displacement at different points from the initial crack tip. Since the crack mouth opening displacement does not reach its critical value, the corresponding cohesive forces do not vanish, as shown in this figure. Finally, the contours of stress distribution σ_x, σ_y, σ_z, τ_{xy}, τ_{xz} and τ_{yz} are shown in Fig. 29 at the final loading step.

6. Conclusion

In the present paper, the three-dimensional cohesive fracture model of non-planer crack growth was presented using the adaptive finite element technique. The 3D cohesive fracture element was developed to simulate the crack propagation in the mixed-mode non-planar curved crack growth. The adaptive finite element technique was implemented through the following three stages; an error estimation, an adaptive mesh refinement, and data transferring. The technique was performed based on the Zienkiewicz–Zhu error estimator using the modified superconvergent patch recovery procedure. The Espinosa–Zavattieri bilinear constitutive equation was employed to evaluate the cohesive tractions and displacement separations. The crack propagation criterion is used in terms of the principal stress and its direction. Finally, in order to demonstrate the validity and capability of proposed computational algorithm, several practical examples were analyzed numerically. Two benchmark examples were chosen to evaluate the performance of adaptive FE strategy for the cohesive crack growth in a bending beam with symmetric and eccentric edge cracks. The next two examples were chosen to illustrate the capability of 3D crack growth in the non-planar curved crack front in complex geometries. The predicted crack growth simulation and corresponding load-displacement curves were compared with the experimental and other numerical results reported in literature. It is shown how the proposed adaptive mesh refinement technique can reduce the value of estimated error considerably in simulation of three-dimensional cohesive crack growth problems.

Acknowledgement

References

Areias, P.M.A., Belytschko, T., 2005. Analysis of three-dimensional crack initiation and propagation using the extended finite element method. Int. J. Numer. Meth. Eng. 63, 760–788.

Barrenblatt, G.I., 1962. The mathematical theory of equilibrium of cracks in brittle fracture. Adv. Appl. Mech. 7, 55–129.

Bažant, Z.P., Planas, J., 1998. Fracture and Size Effect in Concrete and Other Quasibrittle Materials. CRC Press, Boca Raton.

Bouchard, P.O., Bay, F., Chastel, Y., 2003. Numerical modeling of crack propagation: automatic remeshing and comparison of different criteria. Comp. Meth. Appl. Mech. Eng. 192, 3887–3908.

Camacho, G.T., Ortiz, M., 1996. Computational modeling of impact damage in brittle materials. Int. J. Solids Struct. 33, 2899–2938.

Carranza, F.L., Fang, B., Haber, R.B., 1997. A moving cohesive interface model for fracture in creeping materials. Comput. Mech. 19, 517–521.

Chandra, N., Li, H., Shet, C., Ghonem, H., 2002. Some issues in the application of cohesive zone models for metal–ceramic interfaces. Int. J. Solids Struct. 39, 2827–2855.

Dugdale, D.S., 1960. Yielding of steel sheets containing slits. J. Mech. Phys. Solids. 8, 100–104.

Gasser, T.C., Holzapfel, G.A., 2006. 3D Crack propagation in unreinforced concrete: A two-step algorithm for tracking 3D crack paths. Comp. Meth. Appl. Mech. Eng. 195, 5198–5219.

Griffith, A.A., 1920. The phenomena of rupture and flow in solid. Trans. Roy. Soc. Lond. A. 221, 163–197.

Elices, M., Guinea, G.V., Gómez, J., Planas, J., 2001. The cohesive zone model: Advantages, limitations and challenges. Eng. Fract. Mech. 69, 137–163.

Espinosa, H.D., Zavattieri, P.D., 2003. A grain level model for the study of failure initiation and evolution in polycrystalline brittle materials. Part I: Theory and numerical implementation. Mech. Mater. 35, 333–364.

Foulk, J.W., Allen, D.H., Helms, K.L.E., 2000. Formulation of a three-dimensional cohesive zone model for application to a finite element algorithm. Comp. Meth. Appl. Mech. Eng. 183, 51–66.

Geißler, G., Netzker, C., Kaliske, M., 2010. Discrete crack path prediction by an adaptive cohesive crack model. Eng. Fract. Mech. 77, 3541–3557.

Gharehbaghi, S.A., Khoei, A.R., 2008. Three-dimensional superconvergent patch recovery method and its application to data transferring in small strain plasticity. Comput. Mech. 41, 293–312.

Hillerborg, A., Modéer, M., Petersson, P.E., 1976. Analysis of crack formation and crack growth in concrete by means of fracture mechanics and finite elements. Cement Concrete Res. 6, 163–168.

Khoei, A.R., Azadi, H., Moslemi, H., 2008. Modeling of crack propagation via an adaptive mesh refinement based on modified superconvergent patch recovery technique. Eng. Fract. Mech. 75, 2921–2945.

Khoei, A.R., Gharehbaghi, S.A., 2009. Three-dimensional data transfer operators in large plasticity deformations using modified-SPR technique. Appl. Math. Model. 33, 3269–3285.

Khoei, A.R., Gharehbaghi, S.A., Tabarraie, A.R., Riahi, A., 2007. Error estimation, adaptivity and data transfer in enriched plasticity continua to analysis of shear band localization. Appl. Math. Model. 31, 983–1000.

Khoei, A.R., Moslemi, H., Ardakany, K.M., Barani, O.R., Azadi, H., 2009. Modeling of cohesive crack growth using an adaptive mesh refinement via the modified-SPR technique. Int. J. Fract. 159, 21–41.

Krysl, P., Belytschko, T., 1999. Element free Galerkin method for dynamic propagation of arbitrary 3D cracks. Int. J. Numer. Meth. Eng. 44, 767–800.

Lorentz, E., 2008. A mixed interface finite element for cohesive zone models. Comp. Meth. Appl. Mech. Eng. 198, 302–317.

Moës, N., Gravouil, A., Belytschko, T., 2002. Non-planar 3D crack growth by the extended finite element and level sets, Part I. Mechanical model. Int. J. Numer. Meth. Eng. 53, 2549–2568.

Moslemi, H., Khoei, A.R., 2009. 3D adaptive finite element modeling of non-planar curved crack growth using the weighted superconvergent patch recovery method. Eng. Fract. Mech. 76, 1703–1728.

Needleman, A., 1990. An analysis of decohesion along an imperfect interface. Int. J. Fract. 42, 21–40.

Nguyen, O., Repetto, E.A., Ortiz, M., Radovitzky, R.A., 2001. A cohesive model of fatigue crack growth. Int. J. Fract. 110, 351–369.

Oliver, J., Huespe, A.E., Samaniego, E., Chaves, E.W.V., 2004. Continuum approach to the numerical simulation of material failure in concrete. Int. J. Numer. Anal. Meth. Geomech. 28, 609–632.

Ortiz, M., Pandolfi, A., 1999. Finite-deformation irreversible cohesive elements for three-dimensional crack-propagation analysis. Int. J. Numer. Meth. Eng. 44, 1267–1282.

Prasad, M., Krishnamoorthy, C.S., 2001. Adaptive finite element analysis of mode I fracture in cement-based materials. Int. J. Numer. Anal. Meth. Geomech. 25, 1131–1147.

Ruiz, G., Pandolfi, A., Ortiz, M., 2001. Three-dimensional cohesive modeling of dynamic mixed-mode fracture. Int. J. Numer. Meth. Eng. 52, 97–120.

Schrefler, B.A., Secchi, S., Simoni, L., 2006. On adaptive refinement techniques in multi-field problems including cohesive fracture. Comp. Meth. Appl. Mech. Eng. 195, 444–461.

Song, S.H., Paulino, G.H., Buttlar, W.G., 2006. A bilinear cohesive zone model tailored for fracture of asphalt concrete considering viscoelastic bulk material. Eng. Fract. Mech. 73, 2829–2848.

Tvergaard, V., 1990. Effect of fiber debonding in a whisker-reinforced metal. Mat. Sci. Eng. 125, 203–213.

Tvergaard, V., Hutchinson, J.W., 1992. The relation between crack growth resistance and fracture process parameters in elastic–plastic solids. J. Mech. Phys. Solids. 40, 1377–1397.

Tvergaard, V., Hutchinson, J.W., 1996. Effect of strain-dependent cohesive zone model on prediction of crack growth resistance. Int. J. Solids Struct. 33, 3297–3308.

Willis, J.R., 1967. A comparison of the fracture criteria of Griffith and Barenblatt. J. Mech. Phys. Solids 15, 151–162.

Wnuk, M.P., Legat, J., 2002. Work of fracture and cohesive stress distribution resulting from triaxiality dependent cohesive zone model. Int. J. Fract. 114, 29–46.

Zienkiewicz, O.C., Zhu, J.Z., 1992. The superconvergent patch recovery and a posteriori error estimates, Part I. The recovery technique. Int. J. Numer. Meth. Eng. 33, 1331–1364.